Moho beneath Tibet based on a joint analysis of gravity and seismic data

Guangdong Zhao

with Jianxin Liu; Bo Chen; Mikhail K. Kaban

School of Geosciences and Info-physics, Central South University

05 May, 2020, at GFZ, 14473 Potsdam

Outlines

- 1 Forward Method
- 2 Inversion Method
- 3 Numerical Examples
- 4 Moho Structure of the Tibet
- 5 Conclusions

1 Forward Method

1.1 Gravity Forward Modeling for Moho Topography

$$U(x,y,z_0)=G\int_0^X\int_0^Y\int_{h_0}^{h}\frac{\rho(\xi,\eta)}{R}d\xi d\eta d\zeta \quad (1)$$

taking 2D Fourier transform of x and y

$$U(k_x,k_y,z_0)=G\int_0^X\int_0^Y\int_{h_0}^{h}\rho(\xi,\eta)\left\{\int_{-\infty}^{+\infty}\int_{-\infty}^{+\infty}\frac{1}{R}e^{-i\left(k_x x+k_y y\right)}dxdy\right\}d\xi d\eta d\zeta \quad (2)$$

$$U(k_x,k_y,z_0)=2\pi G\int_0^X\int_0^Y\frac{e^{-|k|z_0}}{|k|^2}\rho(\xi,\eta)e^{-i\left(k_x\xi+k_y\eta\right)}\left[e^{|k|h}-e^{|k|h_0}\right]d\xi d\eta \quad (3)$$

expanding $e^{-|k|z0}$ by Taylor series;
taking the vertical derivative

$$\Delta\tilde{g}\left(k_x,k_y,z_0\right)=-2\pi Ge^{-|k|\cdot z_0}\sum_{n=1}^{\infty}\frac{|k|^{n-1}}{n!}\mathcal{F}\left\{\left[h^n(\xi,\eta)-h_0^n\right]\cdot\rho(\xi,\eta)\right\} \quad (4)$$

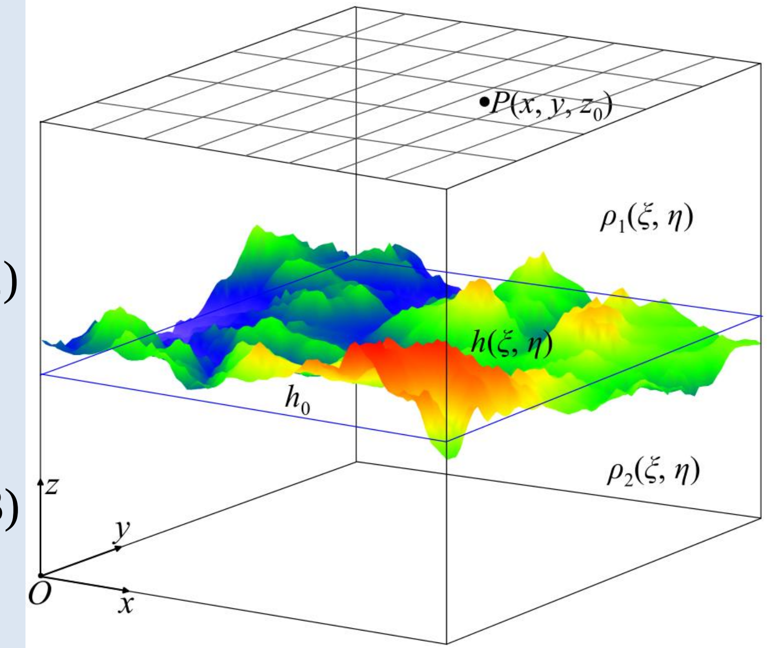

Fig. 1. The coordinate system of a synthetic interface and observation points.

1 Forward Method

1.1 Gravity Forward Modeling for Moho Topography

$$\Delta\tilde{g}\left(k_x,k_y,z_0\right)=-2\pi G e^{-|k|\cdot z_0}\sum_{n=1}^{\infty}\frac{|k|^{n-1}}{n!}\mathcal{F}\left\{\left[h^n(\xi,\eta)-h_0^n\right]\cdot\rho(\xi,\eta)\right\} \quad (4)$$

shifting $e^{-|k|z0}$ in Eq. (3) to the average depth of Moho topography (h_0) instead of 0 in Eq. (4)

$$\Delta\tilde{g}\left(k_x,k_y,z_0\right)=-2\pi G e^{-|k|(z_0-h_0)}\sum_{n=1}^{\infty}\frac{|k|^{n-1}}{n!}\mathcal{F}\left\{\left[h(\xi,\eta)-h_0\right]^n\cdot\rho(\xi,\eta)\right\} \quad (5)$$

Advantages of Eq. (5)

- More stable and accurate than Eq. (4), especially when the exponential term $|k|z_0$ is high;
- Gauss-FFT method is employed instead of the traditional FFT to improve accuracy.

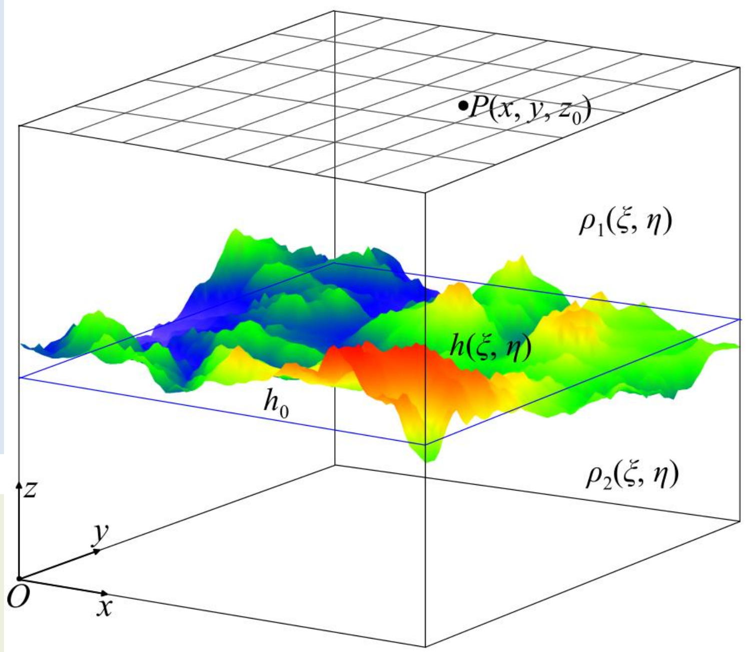

Fig. 1. The coordinate system of a synthetic interface and observation points.

2 Inversion Method

2.1 Gravity inversion for the Moho topography

$$\Delta\tilde{g}\left(k_x,k_y,z_0\right)=-2\pi Ge^{-|k|(z_0-h_0)}\sum_{n=1}^{\infty}\frac{|k|^{n-1}}{n!}\mathcal{F}\left\{\left[h(\xi,\eta)-h_0\right]^n\cdot\rho(\xi,\eta)\right\} \tag{5}$$

by rearranging Eq. (5)

$$\mathcal{F}\left\{\left[h(\xi,\eta)-h_0\right]\cdot\rho(\xi,\eta)\right\}=-\frac{\Delta\tilde{g}e^{|k|(z_0-h_0)}}{2\pi G}-\sum_{n=2}^{\infty}\frac{|k|^{n-1}}{n!}\mathcal{F}\left\{\left[h(\xi,\eta)-h_0\right]^n\cdot\rho(\xi,\eta)\right\} \tag{6}$$

2.2 Joint analysis of gravity and seismic data

- To **mitigate the non-uniqueness** of the gravity inversion,
- Use **seismic-inferred Moho** values as prior information to determine the optimized parameters (the reference depth h_0 and the density contrast ρ),
- By **searching the maximum correlation coefficient** between the gravity-inverted results and the seismic data.

$$\gamma_c = \frac{2S_{12}}{S_1^2 + S_2^2 + (\bar{Y}_1 - \bar{Y}_2)^2} \tag{7}$$

$$\bar{Y}_j = \frac{1}{N}\sum_{i=1}^{N} Y_{ij},\ S_j^2 = \frac{1}{N}\sum_{i=1}^{N}\left(Y_{ij} - \bar{Y}_j\right)^2,\ j = 1, 2;$$
$$S_{12} = \frac{1}{N}\sum_{i=1}^{N}\left(Y_{i1} - \bar{Y}_1\right)\left(Y_{i2} - \bar{Y}_2\right) \tag{8}$$

γ_c: correlation coefficient;

N: the number of the data;

Y_1: gravity-estimated Moho depth; Y_2: seismic-inferred Moho.

3 Numerical Examples

3.1 Forward modeling

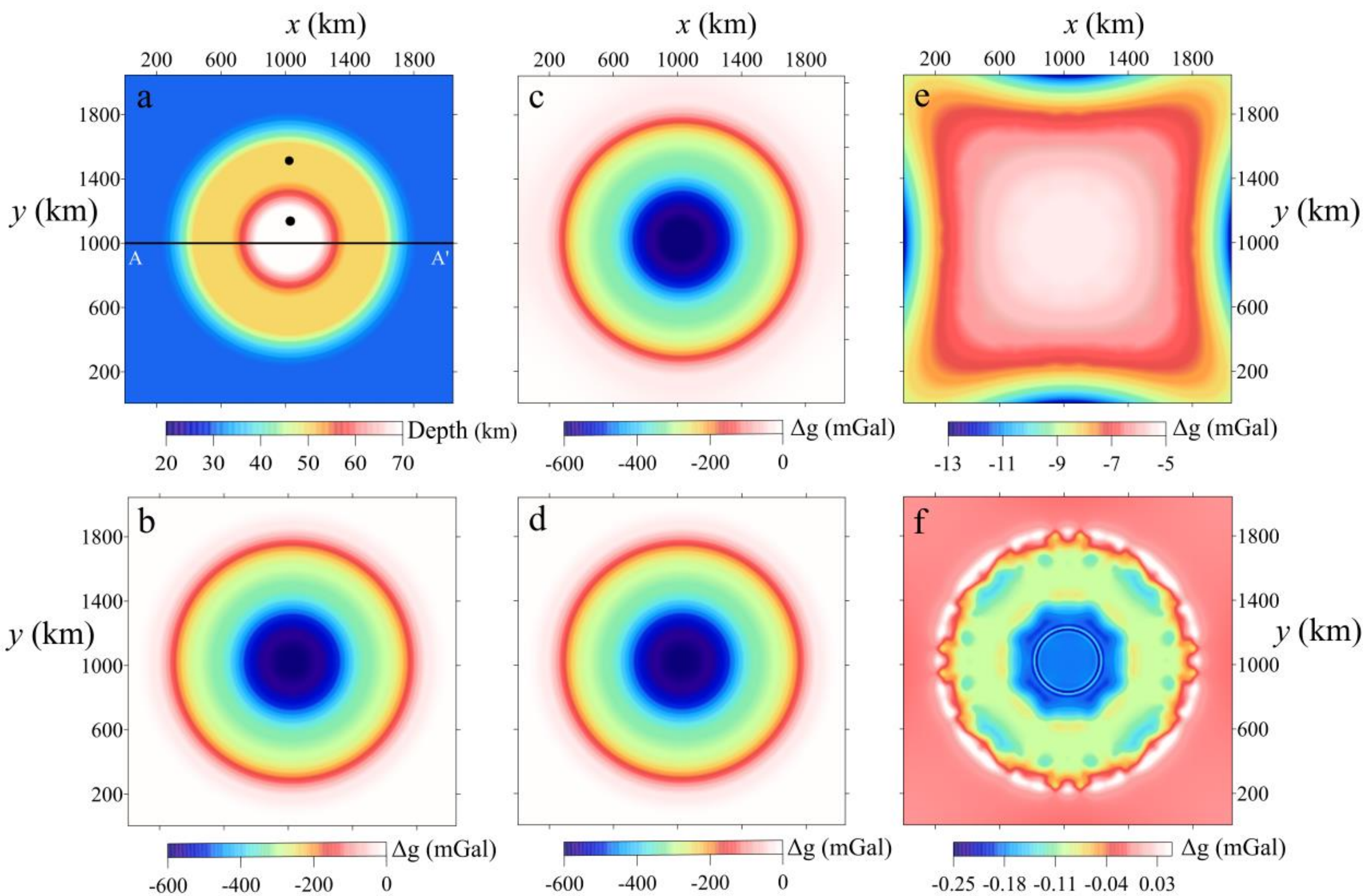

Fig. 2. (a) The synthetic Moho depth; (b) theoretical gravity anomalies observed at 0 *km*; (c) and (d) gravity anomalies obtained from Eq. (4) and (5), respectively; (e) and (f) their differences.

3 Numerical Examples

3.2 Synthetic inversion test

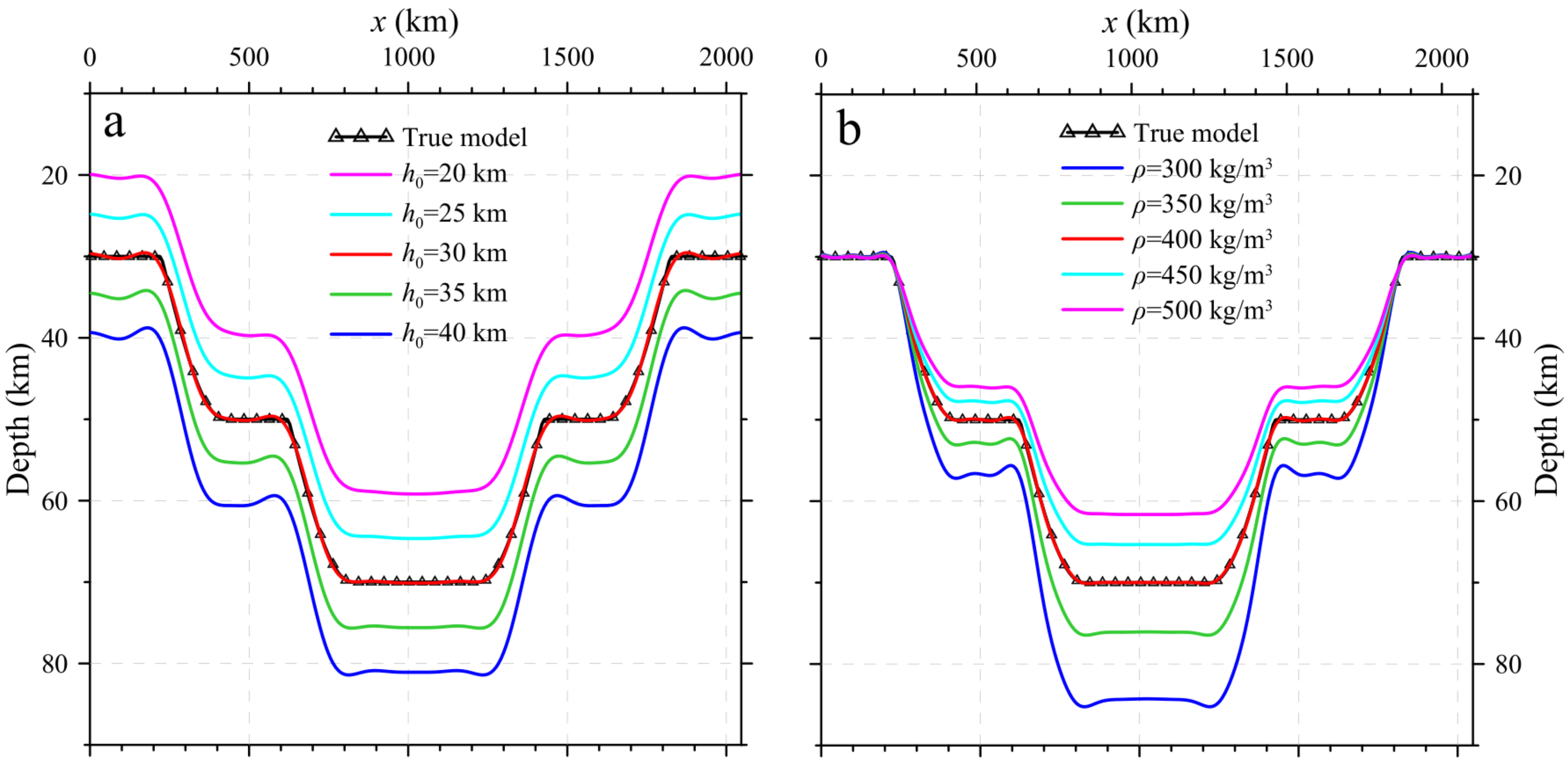

Fig. 3. The inverted Moho undulations for the synthetic model in Fig. 2a based on different reference depths h_0 but true ρ (a) and different density contrasts but true reference depths h_0 (b).

3 Numerical Examples

3.2 Synthetic inversion test

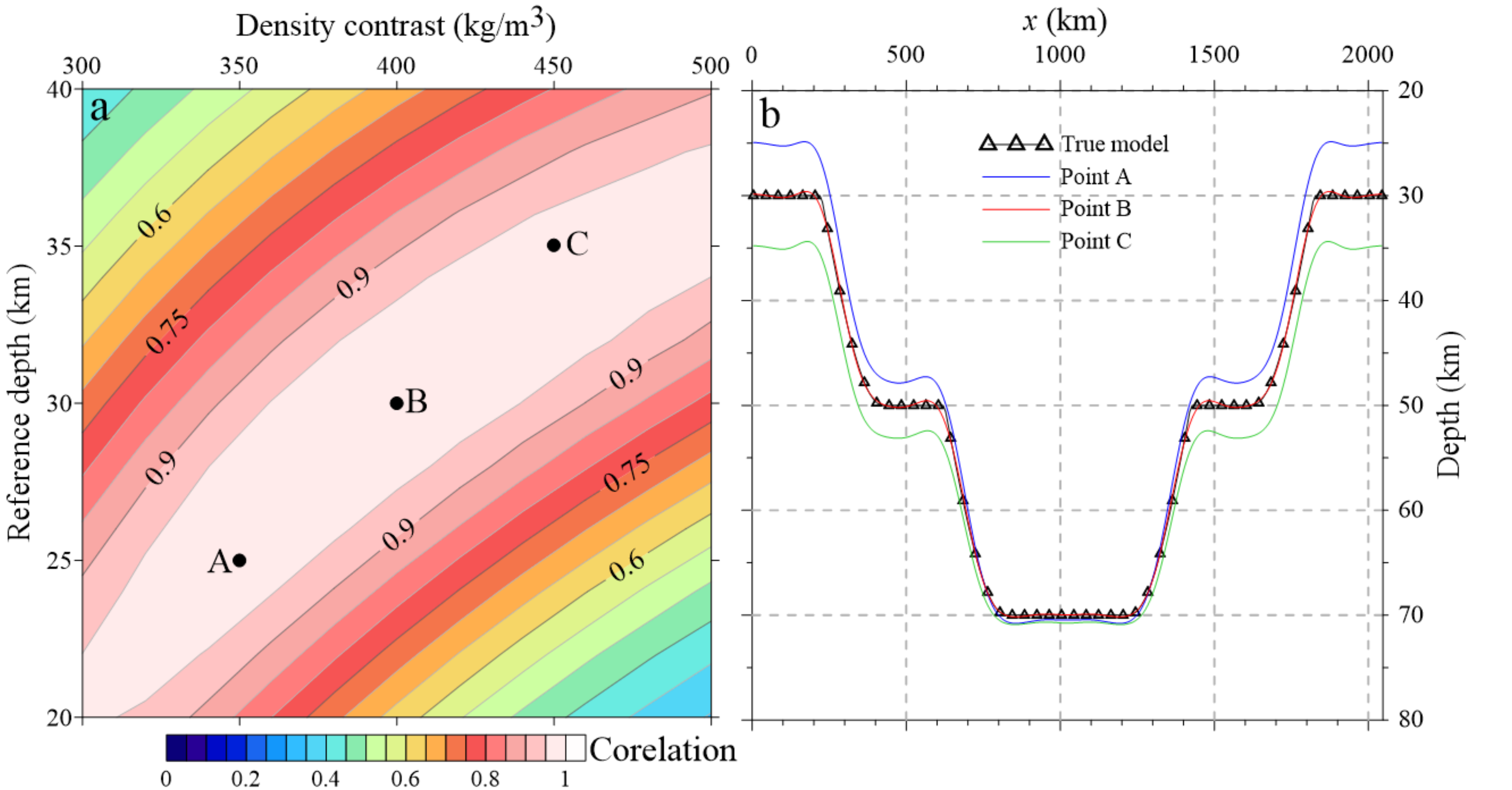

Fig. 4. Distribution of the correlation coefficients (a) and the inversion results on the profile AA' (b) derived by the parameter combinations of points A, B, and C in (a).

4 Moho Structure of the Tibet

4.1 Data

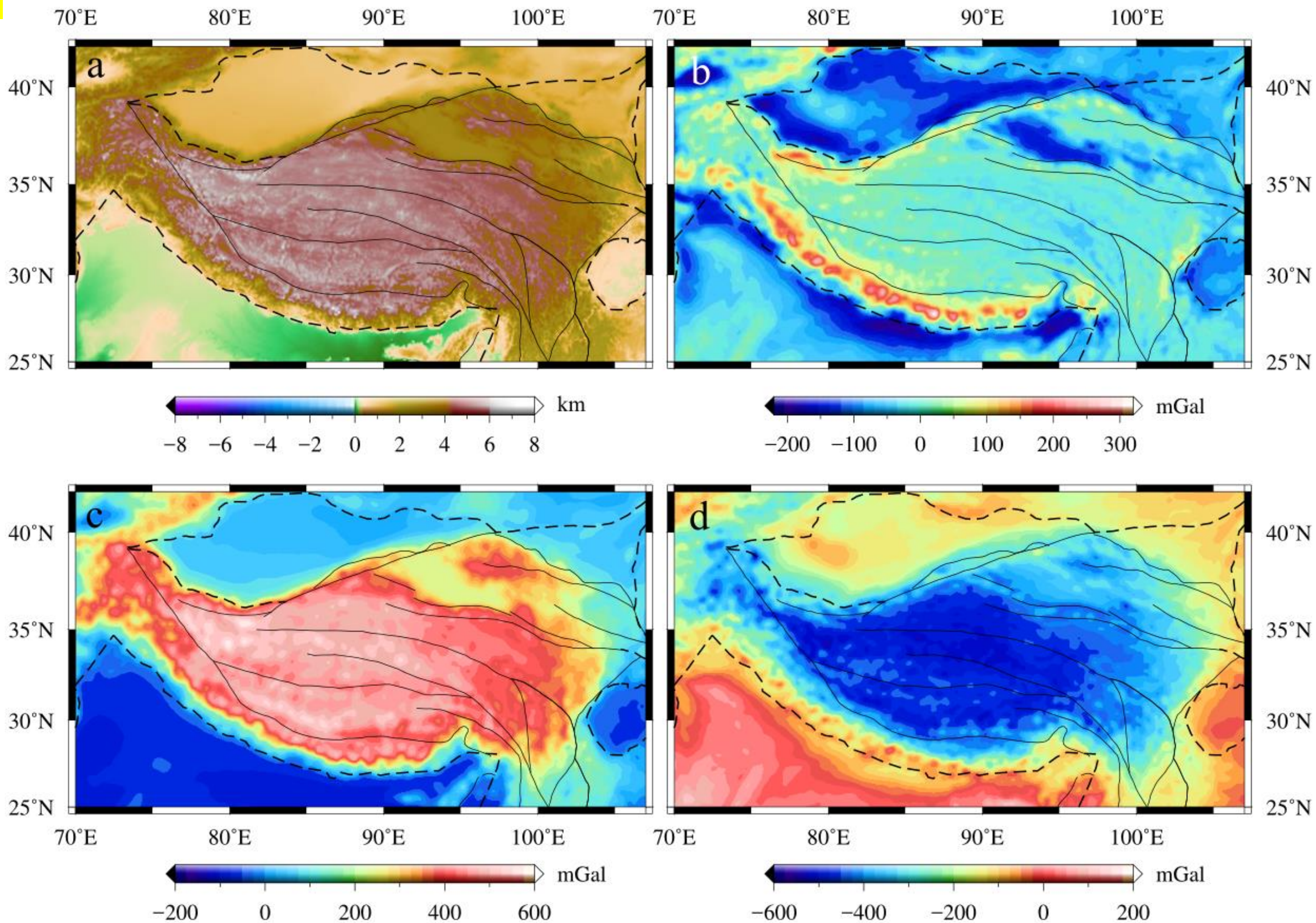

Fig. 5. (a) Topography of the Tibetan Plateau; (b) Free-air gravity disturbances from the EIGEN-6C4 model; (c) Gravity effects of the topography; (d) Bouguer gravity anomalies.

4 Moho Structure of the Tibet

4.1 Data

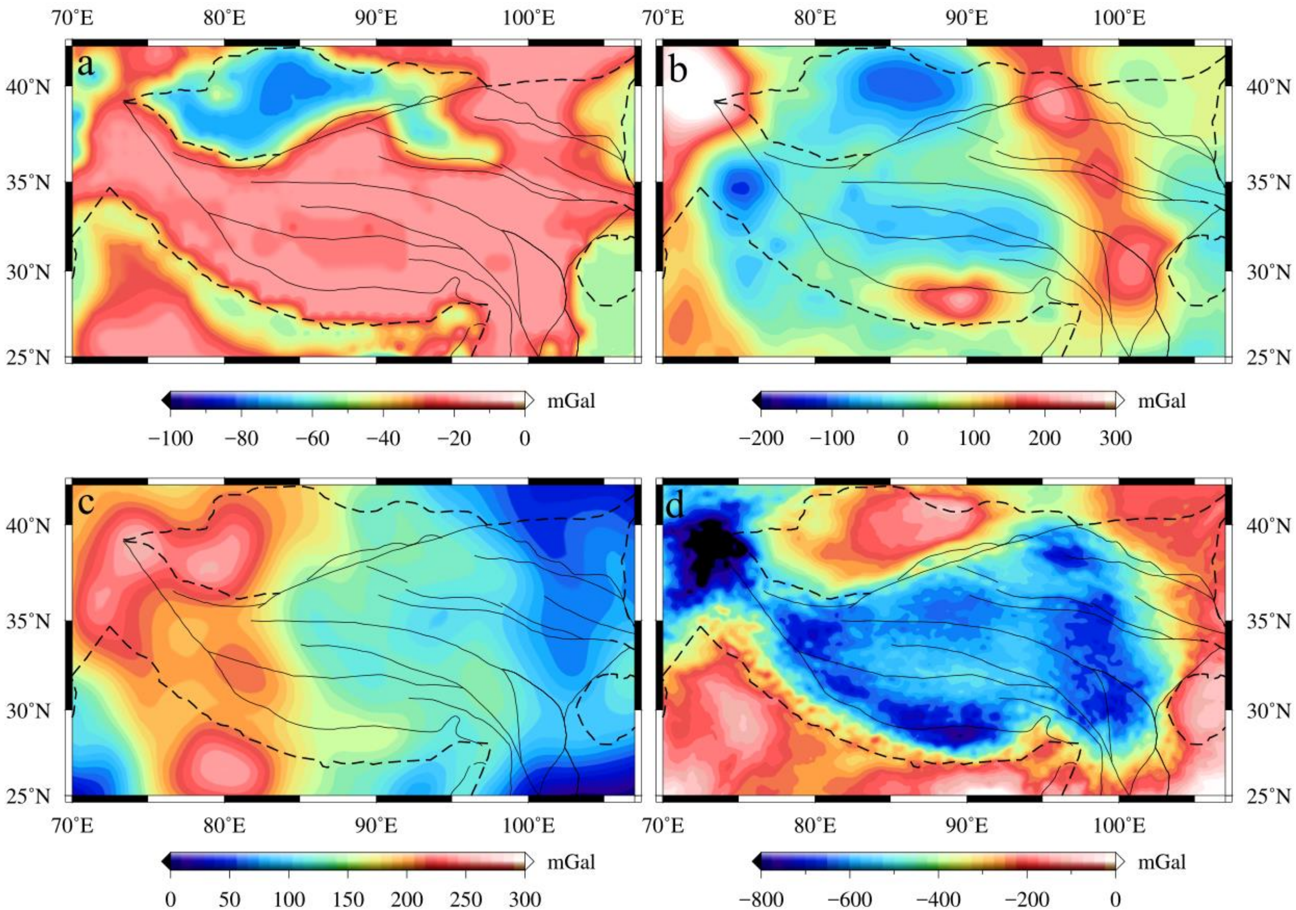

Fig. 6. Gravity effects of (a) sedimentary layers, (b) crystalline crust layers and (c) upper mantle down to 325 km (Kaban et al., 2016). (d) The residual gravity disturbances calculated by removing the effects (Figs. 6a, b, c) from the Bouguer gravity disturbances (Fig. 5d).

4 Moho Structure of the Tibet

4.2 Moho structure beneath Tibet

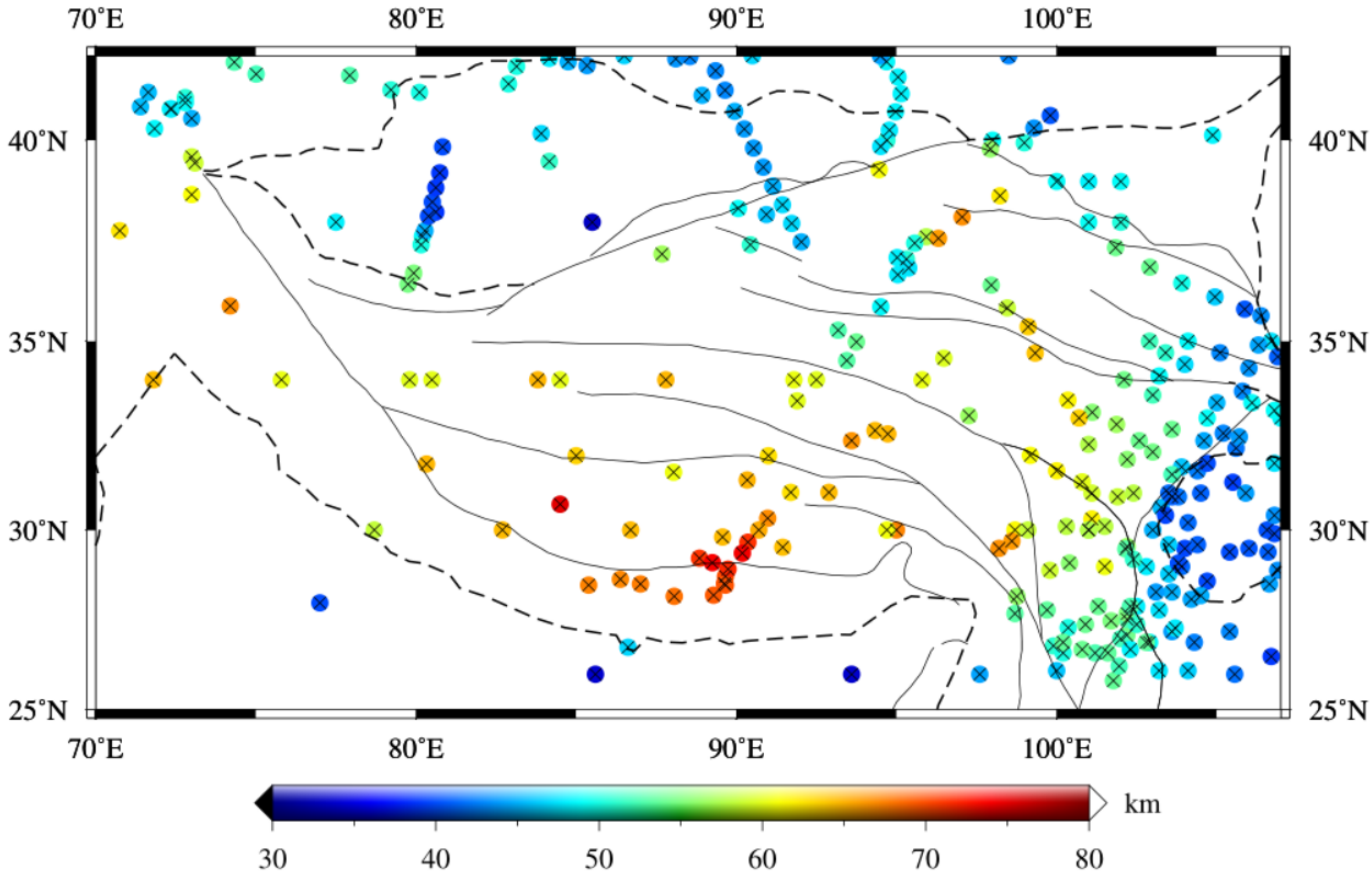

Fig. 7. The Moho depth of the Tibetan Plateau based on the existing seismic determinations compiled by Stolk et al. (2013). Crosses show location of the original seismic data.

4 Moho Structure of the Tibet

4.2 Moho structure beneath Tibet

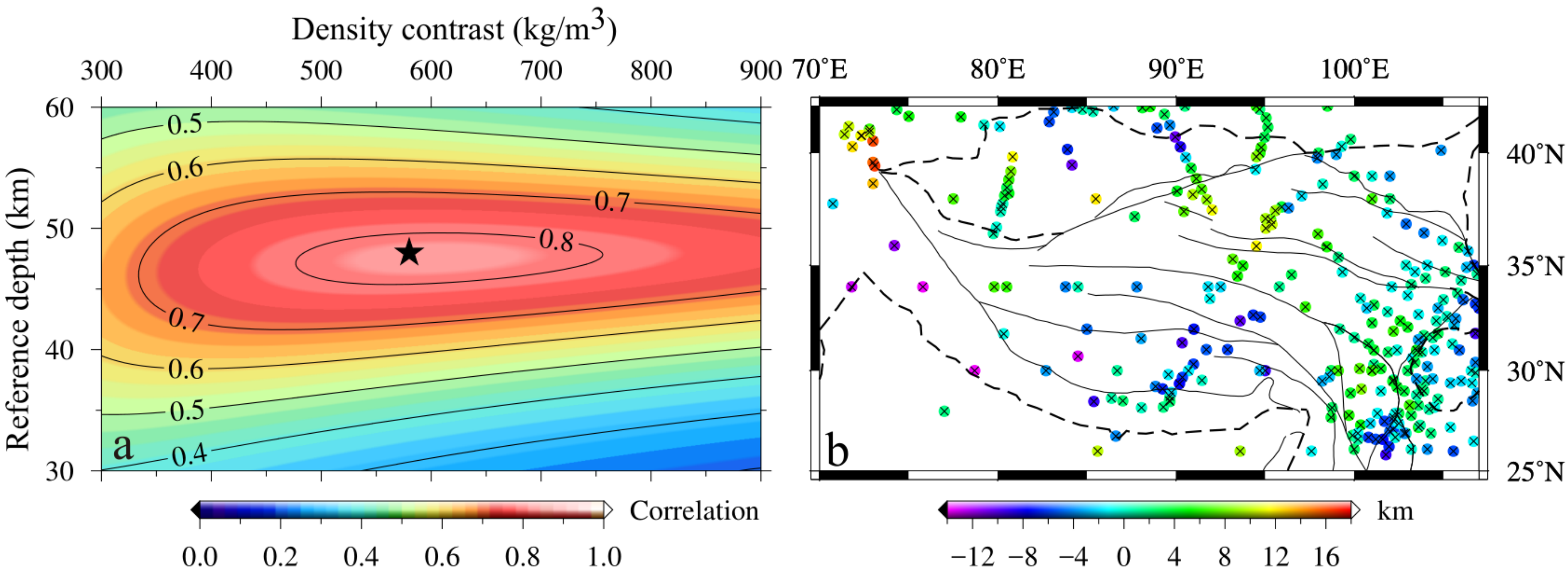

Fig. 8. (a) Correlation coefficients between the Moho depths from Stolk et al. (2013) and our inversion results; (b) Difference between the Moho depths from Stolk et al. (2013) and the inverted Moho for the parameters providing the best correlation with the seismic estimates (h_0 = 48 *km* and ρ = 580 kg/m^3 marked by a star in Fig. 8a).

4 Moho Structure of the Tibet

4.2 Moho structure beneath Tibet

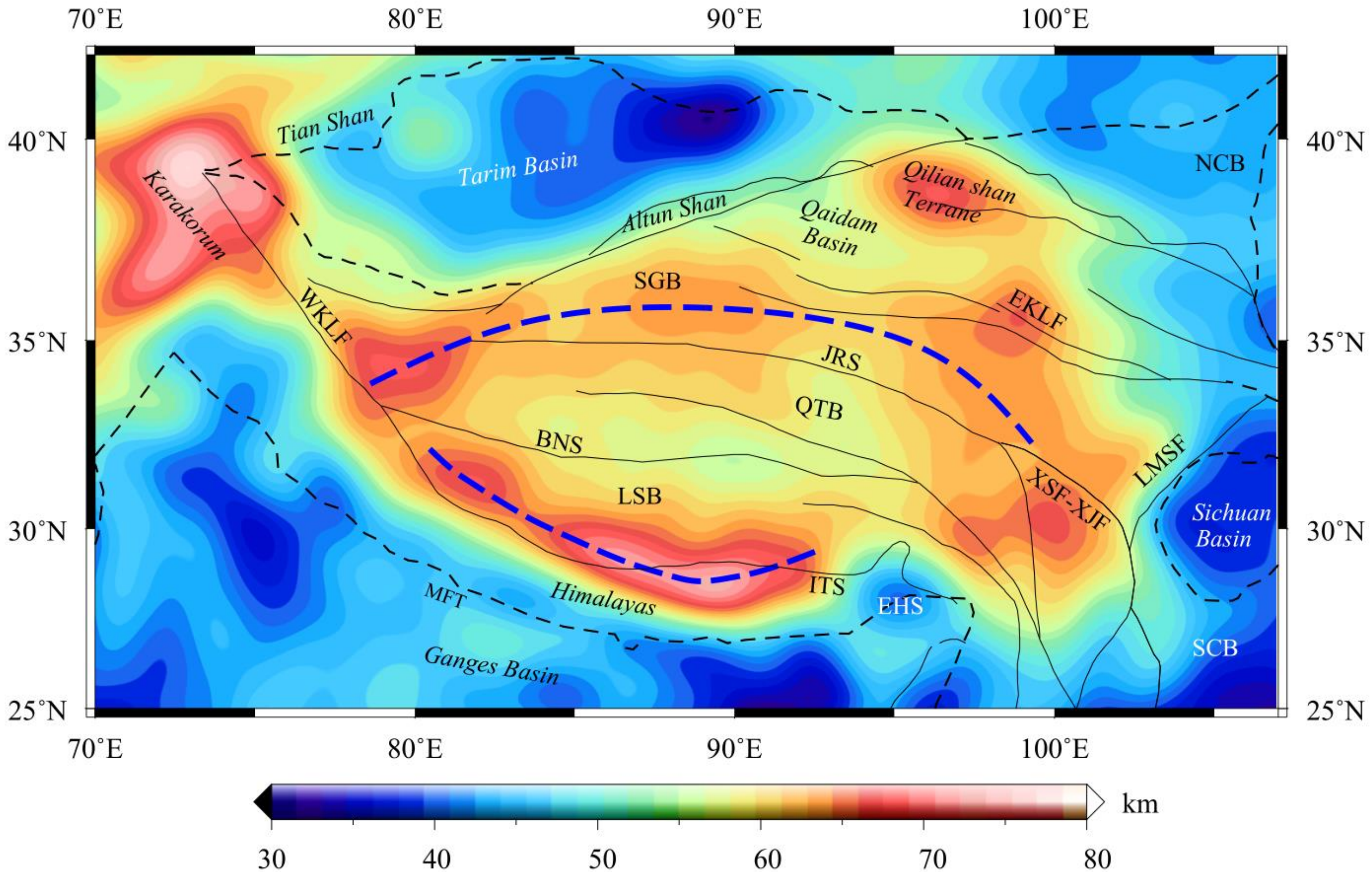

Fig. 9. The inverted Moho topography after the joint inversion with the seismic-estimated Moho depth.

4 Moho Structure of the Tibet

4.3 Discussions

- In the **Indian shield and Ganges basin**, the Moho is **shallow** with a depth of 30 ~ 45 *km*. Here, the shallowest Moho is observed in the northwest and the northeast of the Ganges basin, and south of the MFT;
- Northward, The deeper Moho feature appears as a "**Moho depression belt**" in the southern Lhasa block and the northern Himalayas. We interpret it as a result of the **underthrusting of the Indian lithosphere** beneath Tibet, which is supported by the Hi-CLIMB experiment (Nábělek et al., 2009).
- In central Tibet, the Moho becomes relatively shallow under the northern LSB and southern Qiangtang block. Further to the north, we observe **another "Moho depression belt"** located **beneath the SGB**, which can be explained by the **reverse subduction of the rigid Asian lithosphere** (Willett & Beaumont, 1994; Zhao et al., 2011).

4 Moho Structure of the Tibet

4.3 Discussions

- In northern Tibet, the Moho is **relatively shallow** in the **Qaidam Basin** with a depth of 55 ~ 60 *km*, while it deepens to 68 ~ 70 *km* in the Qilian Shan. In northwest Tibet, the Moho is **30 ~ 50 km** in the **Tarim Basin**.
- In the east of Tibet, the Moho depth is quite shallow with a depth of 35 ~ 40 *km* in the Sichuan Basin.
- Furthermore, the extremely **deep Moho (70 ~ 80 *km*)** is observed beneath the **Karakoram fault region**, which might be related to the deep subduction of the continental lithosphere beneath the Pamir (Burtman & Molnar, 1993; Schneider et al., 2013).

5 Conclusions

- The **improved Parker–Oldenburg's formulas** (with a reference depth and Gauss-FFT method) is used.
- The synthetic models demonstrate that the improved Parker's formula has **higher accuracy** with the maximum absolute error less than 0.25 mGal.
- The seismic-derived Moho depth (Stolk et al., 2013) is used to reduce the non-uniqueness of gravity inversion by the **correlation analysis**.
- In addition to the removal of gravity effects of topography, sediment and crystalline crust, the **upper mantle impact is also removed** based on the seismic tomography model.
- Two visible "**Moho depression belts**" are observed along the Indus-Tsangpo Suture and along the northern margin of Tibet.
- The southern belt might be formed as the **northwards underthrusting** of the Indian plate beneath the Tibetan Plateau, while the northern one is interpreted as the **subduction of the Asian lithosphere**.

References:

•Burtman, V. S., & Molnar, P. H. (1993). Geological and geophysical evidence for deep subduction of continental crust beneath the Pamir (Vol. 281). Geological Society of America.

•Kaban, M. K., Stolk, W., Tesauro, M., El Khrepy, S., Al-Arifi, N., Beekman, F., & Cloetingh, S. A. P. L. (2016). 3D density model of the upper mantle of Asia based on inversion of gravity and seismic tomography data. Geochemistry Geophysics Geosystems, 17(11), 4457-4477.

•Nábělek, J., Hetenyi, G., Vergne, J., Sapkota, S., Kafle, B., Jiang, M., Su, H. P., Chen, J., Huang, B. S., & Team, H.-C. (2009). Underplating in the Himalaya-Tibet Collision Zone Revealed by the Hi-CLIMB Experiment. Science, 325(5946), 1371-1374.

•Oldenburg, D. W. (1974). The inversion and interpretation of gravity anomalies. Geophysics, 39(4), 526-536.

•Parker, R. (1973). The rapid calculation of potential anomalies. Geophysical Journal International, 31(4), 447-455.

•Schneider, F. M., Yuan, X., Schurr, B., Mechie, J., Sippl, C., Haberland, C., ... & Abdybachaev, U. (2013). Seismic imaging of subducting continental lower crust beneath the Pamir. Earth and Planetary Science Letters, 375, 101-112.

•Stolk, W., Kaban, M., Beekman, F., Tesauro, M., Mooney, W. D., & Cloetingh, S. (2013). High resolution regional crustal models from irregularly distributed data: Application to Asia and adjacent areas. Tectonophysics, 602, 55-68.

•Willett, S. D., & Beaumont, C. (1994). Subduction of Asian lithospheric mantle beneath Tibet inferred from models of continental collision. Nature, 369(6482), 642.

•Zhao, W. J., Kumar, P., Mechie, J., Kind, R., Meissner, R., Wu, Z. H., Shi, D. A., Su, H. P., Xue, G. Q., Karplus, M., & Tilmann, F. (2011). Tibetan plate overriding the Asian plate in central and northern Tibet. Nature Geoscience, 4(12), 870-873.

Thanks for your attention !

zgd2015@csu.edu.cn